Strojniški vestnik - Journal of Mechanical Engineering 70(2024)5-6, 259-269
DOI:10.5545/sv-jme.2023.890
Original Scientific Paper
Received for review: 2023-12-07
Received revised form: 2024-03-28
Accepted for publication: 2024-04-11

Multi-response Optimization of GTAW Process Parameters in Terms of Energy Efficiency and Quality

An-Le Van[1] – Thai-Chung Nguyen[2] – Huu-Toan Bui[2] – Xuan-Ba Dang[3] – Trung-Thanh Nguyen[2,*]

[1]Nguyen Tat Thanh University, Faculty of Engineering and Technology, Vietnam
[2]Le Quy Don Technical University, Faculty of Mechanical Engineering, Vietnam
[3]Ho Chi Minh City University of Technology and Education, Vietnam

This work optimizes the current (I), voltage (V), flow rate (F), and arc gap (G) of the gas tungsten arc welding (GTAW) of the Ti40A titanium alloy to decrease the heat input (HI) and improve the ultimate tensile strength (TS) and micro-hardness (MH). The radial basis function network (RBFN) was utilized to present performance measures, while weighted principal component analysis (WPCA) and an adaptive non-dominated sorting genetic algorithm II (ANSGA-II) were applied to estimate the weights and generate optimal points. The evaluation via an area-based method of ranking (EAMR) was employed to determine the best solution. The results indicated that the optimal I, V, F, and G are 89 A, 23 V, 20 L/min, and 1.5 mm, respectively. The improvements in the TS and MH were 1.2 % and 19.8 %, respectively, while the HI was saved by 18.4 %. The RBFN models provided acceptable accuracy for prediction purposes. The ANSGA-II provides better optimality than the conventional NSGA-II. The HI, TS, and MH of the practical GTAW Ti40A could be enhanced using optimality. The optimization method could be utilized to deal with optimization problems for not only other GTAW operations but also other machining processes.

Keywords: GTAW, Heat input, Ultimate tensile strength, Micro-hardness, radial basis function network

Highlights

- *Optimizing GTAW operation considering the heat input, ultimate tensile strength, and micro-hardness.*
- *A radial basis function network is utilized to propose the GTAW performance measures.*
- *Process parameters, including the current, voltage, flow rate, and arc gap, were optimized.*
- *An adaptive non-dominated sorting genetic algorithm II was proposed and applied.*

0 INTRODUCTION

Gas tungsten arc welding (GTAW) is a popular welding method that joins metals with a non-consumable electrode. It involves heating the metal to produce a weld pool by creating an arc between the electrode and the specimen. A shielding gas keeps the weld area safe from airborne contaminants. GTAW produces high-quality welds, exact control, excellent weld penetration, minimal spatter, and a variety of metals.

Different GTAW operations have been considered and optimized to enhance the performances measured. For the GTAW Inconel 718 alloy, response surface method (RSM) models of the bead width (*BW*), depth of penetration (*DP*), heat-affected zone (*HAZ*), and area of the fusion zone were developed [1]. The authors stated that weld bead properties were mostly impacted by the welding current (*I*) and torch speed (*S*), respectively. The *BW*, Brinell hardness (*BH*), and micro-hardness (*MH*) were improved for the welded Inconel 625 using the grey relational analysis and TOPSIS [2]. The results presented that the optimal *I, S*, and arc gap (*G*) were 300 A, 90 mm/min, and 5 mm, respectively. In terms of the *I, S,* and *G*, the *DP* and *BW* models of the titanium joints were proposed [3]. The authors claimed that to create TWB joints free of defects, the ideal parameters of 135 A, 4.1 mm/s, and 3 mm may be used. An aspect ratio of 0.421 and the ideal hardness of 262 HB of the welded Inconel 625 could be generated at I = 300 A, S = 75 mm/min, and G = 1 mm using the TOPSIS [4]. For the welded 5052 alloys, predictive models were provided in terms of the *I, V,* and *S* for the penetration shape factor, *MH,* and reinforcement form factor of the weld specimens [5]. The optimal *I*, *V*, and *S* reported were 140 A, 18 V, and 300 mm/min, respectively. The *BW* and *DP* models of the welded AISI316L were proposed in terms of the *I* and *S*, in which the PSO was used to find the best ANN model [6]. The small deviations (less than 4 %) indicated that the developed correlations were efficiently used in the GTAW operation. Wan et al. find that the tensile strength (*TS*) and elongation (*EL*) could be improved using the optimized weld shape [7]; the *TS* and *EL* of the welded 2219-T8 aluminium alloys were enhanced by 70 % and 4 %, respectively. Vijayakumar et al. [8] presented that the peak current of 50 A, inter-pulse current of 30 A, and inter-pulse frequency of 20 kHz could be used to improve the characteristics of the IP-TIG welded Ti6Al4V alloy. The RSM model of the joint strength was developed for the IN-718 weld by Sonar

*Corr. Author's Address: Le Quy Don Technical University, 236 Hoang Quoc Viet, Ha Noi, VietNam, trungthanhnguyen@lqdtu.edu.vn

et al. [9], who found that the developed weld exhibited 32 % higher strength and superior corrosion resistance than TIG ones. The RSM models of the maximum yield strength and *EL* were developed for the IP-TIG welded Alloy 718 joints [10]. The authors stated the yield strength and *EL* of the IP-TIG joint were 94.5 % and 82.9 % of base metal, respectively. The ANOVA is used to determine the optimal values of the GTAW mild steel plates [11]. The maximum impact strength was obtained at the *I* of 158.605, a notch angle of 59°, and a single pass, respectively. A convolutional neural network was used to train the *BW* and *DP* models [12]. The R^2 value of 0.998 indicated that the developed models could be used to control the quality in real time. The Taguchi and RSM were used to enhance the *TS* of the welded SS316L stainless steel pipes [13]; the optimal working cycle and peak current were 66.5 % and 114.7 A, respectively. Deep learning was proposed to predict the *DP* value [14]. The low error level showed that the developed models can be utilized in the GTAW process. Pandya et al. [15] indicated that oxide flux increased the weld penetration and mechanical strength of welded 2205 duplex stainless steel. Moreover, the *DP* of 6.23 mm, *TS* of 775 MPa, and *MH* of 322 HV were obtained using the RSM. Similarly, Baskoro et al. presented that the *DP* and *TS* of the welded 304 stainless steel could be increased by 89.9 % and 17.2 %, respectively, with the SiO_2 flux [16].

However, the limitations of related works can be expressed as follows.

The mechanical and shape characteristics are frequently taken into account, while the heat input has not been discussed. Reducing the heat input will help the GTAW operate more energy-efficiently.

The RSM is widely used to propose performance models, while the application of the ANN has been rare. Moreover, the *HI*, *TS*, and *MH* models have not been developed for the GTAW Ti40A plates.

The impacts of GTAW process parameters on the *HI*, *TS*, and *MH* have not been analysed.

The optimal GTAW parameters have not been selected to improve the HI, TS, and MH simultaneously.

The Taguchi and RSM methods are highly likely to find local outcomes. Therefore, an efficient approach to finding global data is necessary.

1 OPTIMIZING FRAMEWORK

The *HI* is defined as a ratio of energy consumption per length and computed as:

$$HI = \frac{\eta \times I_i \times V_i}{S}, \tag{1}$$

where I_i, V_i, S, and η are the instant current, instant voltage, torch speed, and thermal efficiency, respectively.

The *TS* is computed as:

$$TS = \frac{\sum_{i=1}^{n} TS_i}{n}, \tag{2}$$

where TS_i and n are the tensile strength of the i^{th} sample and the number of samples, respectively.

The *MH* is computed as:

$$MH = \frac{\sum_{i=1}^{n} MH_i}{n}, \tag{3}$$

where MH_i and n are the micro-hardness of the i^{th} location and the number of positions, respectively.

Table 1. *Process parameters of the GTAW operation*

Parameters	Levels
Current, *I* [A]	70, 90, 110, 130
Voltage, *V* [V]	22, 23.5, 25, 26
Flow rate, *F* [L/min]	12, 15, 17, 20
Arc gap, *G* [mm]	1.5, 2.5, 3.5, 4.5

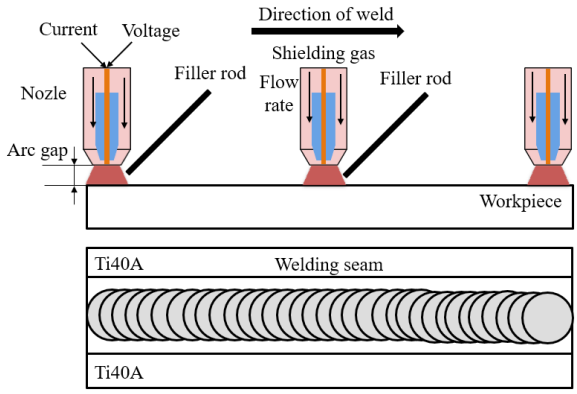

Fig. 1. *The scheme of the GTAW process*

Fig. 1 illustrates the GTAW process. Table 1 displays the process parameters with their respective levels. The machine's manufacturer's recommendations are used to calculate the values of *I* and *V*. The *F* is chosen in accordance with the attributes of the air supplier, whilst the *G* is cited from relevant sources. The optimization issue is expressed as:

Finding $X = [I, V, F, \text{and } G]$.

Maximizing *TS* and *MH*; Minimizing *HI*.

Constraints: 70 A ≤ *I* ≤ 130 A; 22 V ≤ *V* ≤ 26 V;

12 L/min ≤ *F* ≤ 16 L/min; 1.5 mm ≤ *G* ≤ 4.5 mm.

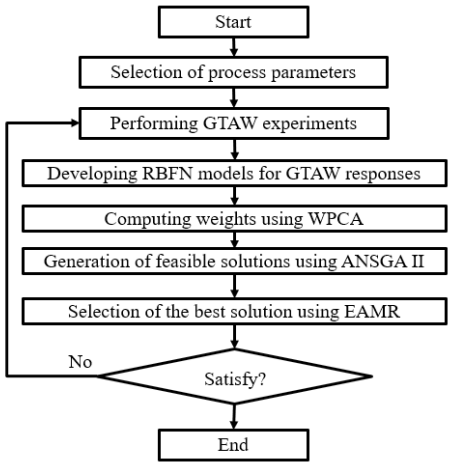

Fig. 2. *Optimization approach for the GTAW*

Fig. 2 shows the optimization framework for the GTAW operation.

Step 1: Use the L_{32} orthogonal array to conduct GTAW experiments **[17]**.

Step 2: The RBFN models of the outputs are developed regarding GTAW parameters **[18]**.

The RBFN with Gaussian function is used to present the correlations between the inputs and outputs. The input parameters are combined into the hidden one, while the output for the given input (s) and vector (c_i) is expressed as:

$$out_i = \exp\left(-\frac{1}{2\sigma^2}\left\|s-c_i\right\|^2\right), \tag{4}$$

where $\|s_i - c_i\|$ is the Euclidean distance between s and c_i.

The Gaussian function is expressed as:

$$\Phi(r) = \exp\left(-\gamma r^2\right), \tag{5}$$

where γ is a parameter that is found using the cross-validation stage.

The RBFN model for a given input s is expressed as:

$$out = w_0 + \sum_{i=1}^{m} w_i \exp\left(-\frac{1}{2\sigma^2}\left\|s-c_i\right\|^2\right), \tag{6}$$

where w_0 and w_m are the bias and weight, respectively.

Step 3: The WPCA is used to compute the weights.

The normalized response (n_r) is computed as:

$$n_r = \frac{R_i(m)}{\sum_{1}^{n} R_i(m)}. \tag{7}$$

The correlative data (S_{jl}) is computed as:

$$S_{jl} = \left[\frac{Cov\left(R_i(j), R_i(l)\right)}{\sigma_{Ri}(j)\times\sigma_{Ri}(\mathrm{l})}\right], \tag{8}$$

where $Cov(R_i(j)$ *and* $Ri(\mathrm{l}))$ denote the covariance of sequences $I_i(j)$ and $I_i(l)$, respectively.

Eigenvalues (λ_k) and eigenvectors (V_{ik}) are computed as:

$$(S-\lambda_k J_m)V_{ik} = 0. \tag{9}$$

The major principal coefficient is computed as follows:

$$PC_m = \sum_{i=1}^{n} I_m(i)\times V_{ik}. \tag{10}$$

Step 4: The ANSGA-II is used to find solutions.

The adaptive crossover probability and adaptive mutation probability are used in the ANSGA-II to identify the best solutions. Fig. 3 illustrates how the ANSGA-II operates.

- Producing initial population $X(0)$ and computing the function value $f(x)$ for each individual.
- The middle generation $X'(t)$ is created by performing the adaptive crossover and mutation operators.
- When an individual's fitness exceeds the average, they can be passed on to the next generation, which lowers the crossover probability (p_c) and mutation probability (p_m). However, if an individual's fitness level is lower than the average, they may be removed, which would result in greater p_c and p_m levels. The crossover and mutation operations' equations are written as follows:

$$p_c = \begin{cases} p_{c1} - \dfrac{p_{c1}-p_{c2}}{f_{\max}-f_{avg}}(f'-f_{avg}) \\ p_{c1} \end{cases}, \tag{11}$$

$$p_m = \begin{cases} p_{m1} - \dfrac{p_{m1}-p_{m2}}{f_{\max}-f_{avg}}(f'-f_{avg}) \\ p_{m1} \end{cases}. \tag{12}$$

- Creating a new non-dominate set $P'(t)$ by joining the non-dominate solutions.
- To create a new population $X(t+1)$, randomly generate new individuals and join them to the non-dominated solutions.

Step 4: The EAMR is used to select the best optimality.

The positive solution is computed as:

$$S_i^+ = v_{i1}^+ + v_{i2}^+ + v_{i3}^+ + ...v_{im}^+. \quad (13)$$

The negative solution is computed as:

$$S_i^- = v_{i1}^- + v_{i2}^- + v_{i3}^- + ...v_{im}^-. \quad (14)$$

The performance indicator (I_i) is computed as:

$$I_i = \frac{S_i^+}{S_i^-}. \quad (15)$$

The best solution is selected with the highest I_i.

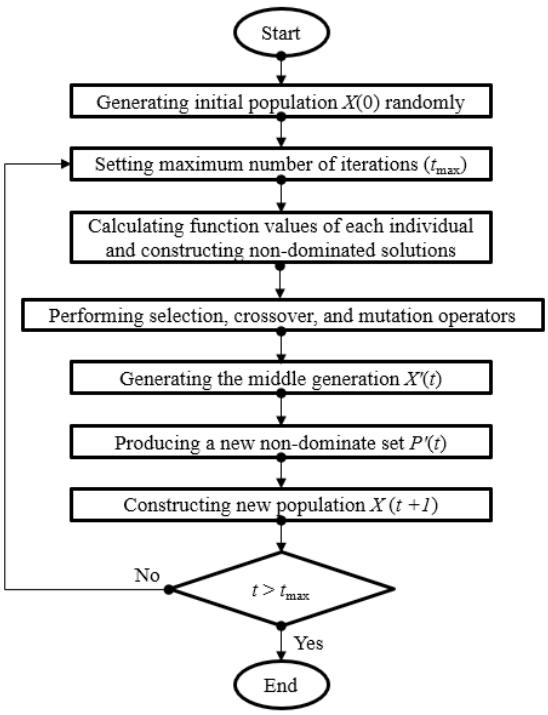

Fig. 3. *The operating principle of the ANSGA-II*

2 EXPERIMENTAL FACILITIES

Using the WEDM method, the specimens are sliced from the Ti40A plates and then cleaned using carbide sheets. The measurements of each specimen are 3 mm in thickness, 64 mm in width, and 80 mm in length. The anti-corrosion cover of the marine ship is mostly made of welded Ti40A plates. Each filler stick has the following measurements: 8 mm for length, 2 mm for breadth, and 3 mm for thickness. The chemical compositions of the Ti40A are shown in Table 2.

All testing is conducted using a ZX7-200 welding machine and a designed fixture (Fig. 4). During the processing stage, two welded layers are produced to enhance the junction. Tensile and micro-hardness tests were conducted using the Exceed E45 and Wilson hardness machines, respectively. The instantaneous voltage and current are measured using the clamp meter known as PAC22.

Fig. 4. *Experiments of the GTAW operation*

Table 2. *Chemical compositions of the Ti40A*

Element	Fe	O	C	N	H	Other	Ti
[%]	0.30	0.25	0.08	0.03	0.015	0.05	Balance

Figs. 5 and 6 display the representative values obtained at experimental No. 3 and 31, respectively.

As shown in Fig. 7, the microstructure of the various welding locations, such as the base material (BM), heat-affected zone (HAZ), and welded zone (WZ), are examined. Fig. 7a displays the BM's microstructure with large particles and irregular dimensions in comparison to the preceding sections. In the welded zone, the grain size is approximately 170 µm. The uniformly fine grain (about 15 µm) without any faults, such as flash, fractures, voids, and porosity, is produced in the welded region (Fig. 7a). In Fig. 7b, the coarser grain and uneven size of the heat-affected zone (HAZ) are detected without any flaws, including voids and pits. Because of the heat from the welding, the grain size in the HAZ is about 105 µm.

3 RESULTS AND DISCUSSIONS

3.1 Impacts of Process Parameters on Responses

The experimental data of the GTAW Ti40A are shown in Table 3.

As the *I* increases from 70 A to 130 A, the *HI* is increased by 52.6 % (Fig. 8a). An increased *I* causes

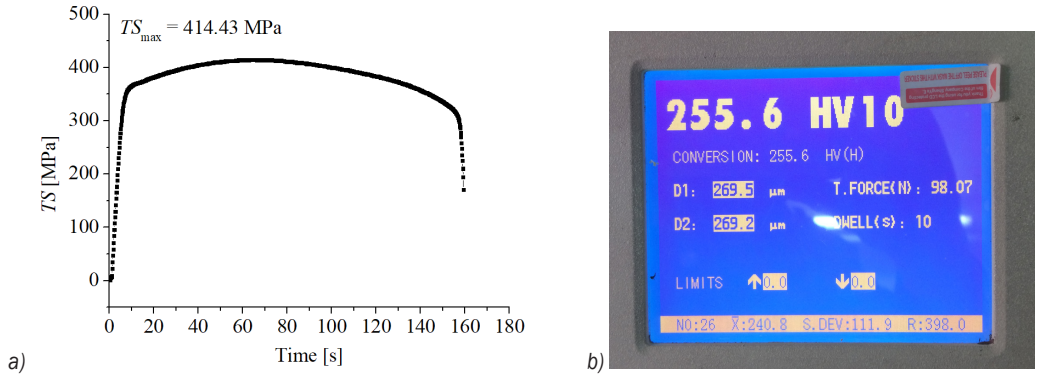

Fig. 5. *Experimental outcomes at the No. 3; a) tensile strength, and b) micro-hardness*

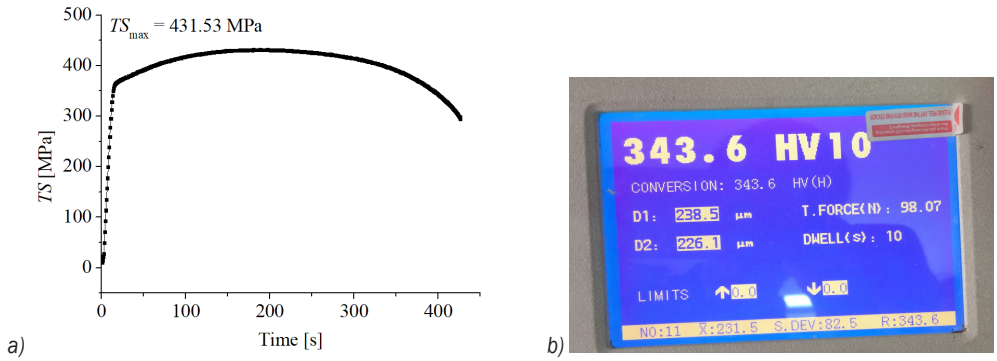

Fig. 6. *Experimental outcomes at the No. 31; a) tensile strength, and b) micro-hardness*

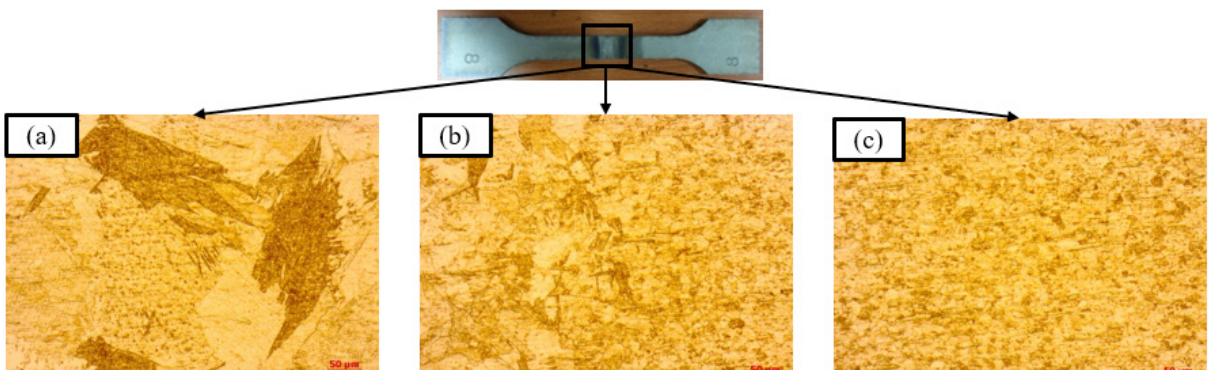

Fig. 7. *Analysis of the micro-structure of different zones*

a higher instant current; hence, more heat input is produced. As *V* increases from 22 V to 26 V, the *HI* is increased by 39.2 % (Fig. 8a). An increased *V* causes a higher arc voltage, leading to higher heat input. The similar impacts of the *I* and *V* on the *HI* were explained in the works of [7], [15], and [16]. As *F* increases from 12 L/min to 20 L/min, the *HI* is decreased by 24.3 % (Fig. 8b). A higher *F* increases the amount of shielding gas, leading to a reduction in the instant current; hence, the *HI* reduces. As the *G* increases from 1.5 mm to 4.5 mm, the *HI* is decreased by 21.3 % (Fig. 8b). A higher *G* increases the electrode stick out, leading to a higher resistance. The instant current decreases, and the *HI* decreases. Similar influences can be found in the literature [19].

The *TS* improves by 18.6 % when the *I* rises from 70 A to 130 A (Fig. 9a). Due to the poor diffusion between the two plates caused by the low energy input supplied at a low *I*, a low *TS* was formed. A greater *I* results in a better fusion and an improvement in the *TS* by increasing the energy delivered to the base metal. As *V* increases from 22 V to 24 V, the *TS* is increased

Table 3. *Experimental results of the GTAW operation*

No.	*I* [A]	*V* [V]	*F* [L/min]	*G* [mm]	*HI* [J/mm]	*TS* [MPa]	*MH* [HV]
Experimental data for developing the models							
1	70	22	12	1.5	762.19	408.68	254.2
2	90	23.5	12	2.5	780.52	427.87	266.5
3	110	25	12	3.5	857.51	431.53	255.6
4	130	26	12	4.5	980.14	432.28	232.7
5	70	23.5	12	1.5	842.05	436.40	251.1
6	90	22	12	2.5	698.62	402.24	273.6
7	110	26	12	3.5	888.90	416.15	238.2
8	130	25	12	4.5	947.38	449.05	252.9
9	90	25	15	1.5	797.86	468.61	259.7
10	70	26	15	2.5	745.81	424.55	253.9
11	130	22	15	3.5	765.12	457.12	273.3
12	110	23.5	15	4.5	680.93	448.88	301.4
13	90	26	15	1.5	826.23	455.23	245.3
14	70	25	15	2.5	716.91	437.75	267.9
15	130	23.5	15	3.5	848.64	479.46	258.2
16	110	22	15	4.5	596.62	426.35	315.9
17	130	22	17	1.5	693.12	479.76	256.8
18	110	23.5	17	2.5	718.72	468.79	279.5
19	90	25	17	3.5	656.18	438.71	288.9
20	70	26	17	4.5	493.63	400.91	294.9
21	130	23.5	17	1.5	772.97	503.87	244.1
22	110	22	17	2.5	637.94	444.34	291.5
23	90	26	17	3.5	685.98	424.17	271.5
24	70	25	17	4.5	463.31	415.23	311.9
25	110	25	20	1.5	729.35	469.54	274.1
26	130	26	20	2.5	870.87	458.71	219.3
27	70	22	20	3.5	388.56	388.73	354.4
28	90	23.5	20	4.5	493.01	422.25	349.7
29	110	26	20	1.5	756.91	455.38	256.4
30	130	25	20	2.5	841.92	474.27	239.8
31	70	23.5	20	3.5	468.43	414.76	344.1
32	90	22	20	4.5	411.09	398.31	364.2
Experimental data for testing models							
33	90	22	20	4.5	411.09	398.31	364.2
34	80	24	13	3	711.62	424.53	272.4
35	100	23	14	2	739.42	455.12	271.8
36	120	24.5	16	4	804.95	467.22	268.6
37	75	24	18	2	649.06	452.62	302.3
38	85	22.5	19	3	524.92	421.51	329.2
39	95	25.5	13	4	741.25	414.83	266.1
40	105	24.5	16	2	769.22	474.26	263.7
41	115	25	18	3.5	779.18	459.98	267.5
42	95	22	19	4.5	450.74	408.80	351.7
43	105	23	20	3	629.07	440.35	316.3
44	95	25.5	15	2	803.78	456.12	252.2
44	120	23.5	18	3.5	748.98	467.86	283.3
45	130	24	16	4.5	851.04	479.81	270.4
46	105	26	17	3	778.37	442.05	251.8
47	90	24	15	3	688.59	444.37	283.4

by 9.4 %, while a further *V* decreases by around 5.3 % in the *TS* (Fig. 9a). A weak joint is created because a low *V* causes a low heat input and a poor specimen combination. The heat input rises with a *V* increase, strengthening the joint. A further *V*, however, transfers too much energy into the base material. The overheating temperature may lead to a higher grain size; hence, the *TS* decreases. Similar impacts of the *I* and *V* can be found in the works of **[7]**, **[13]**, and **[16]**.

As *F* increases from 12 L/min to 16 L/min, the *TS* is increased by 7.5 %, while a further *F* decreases by around 11.1 % in the *TS* (Fig. 9b). A higher *F* may cause a proper welding condition, leading to a lower grain size; hence, the *TS* decreases. However, an excessive *F* decreases the heat input transferred into the base material, leading to an improper fusion; hence, a weak joint is produced. As the *G* increases from 1.5 mm to 4.5 mm, the *TS* is reduced by 10.1 % (Fig. 9b). Higher *G* results in an incorrect fusion due to lower input energy transferred to the base material; hence, the *TS* decreases. The welding gap length and the energy input have an inverse relationship. Consequently, at the lowest *G*, the *TS* can be maximized. Similar results were presented in the literature **[20]**.

The *MH* decreases by 23.3 % when the *I* rises from 70 A to 130 A (Fig. 10a). A rise in the *I* causes the energy input at the welding zone to increase, which raises the grain size and causes the *MH* to drop. The *MH* decreases by 22.5 % when *V* rises from 22 V to 24 V (Fig. 10a). A rise in the *V* results in a higher energy input, which in turn leads the welding area to become coarser; as a result, the *MH* reduces. Similar results were presented in the literature **[5]** and **[20]**.

The *MH* rises by 23.2 % when *F* increases from 12 L/min to 16 L/min (Fig. 10b). A greater *F* is linked to lower energy input, which causes solidification to happen more quickly and produces a higher *MH*. The *MH* increases by 18.5 % as *G* increases from 1.5 mm to 4.5 mm (Fig. 10b). Higher heat input at a low *G* could result in larger grain sizes and a low *MH*. Lower energy input results from a higher *G*. The result is a tiny grain size, which raises the *MH*. Similar outcomes can be found in the work of **[20]**.

3.2 ANOVA Analysis for Welding Responses

ANOVA results for the *HI* model are shown in Table 4. The *I, V, F, G, IF, VG, FG,* I^2, V^2, F^2, and G^2 are significant terms for the *HI* model. The contributions of the *I, V, F*, and *G* are 22.32 %, 15.38 %, 13.31 %, and 11.12 %, respectively. The contributions of the *IF, UG,* and *FG* are 3.43 %, 14.44 %, and 3.83 %,

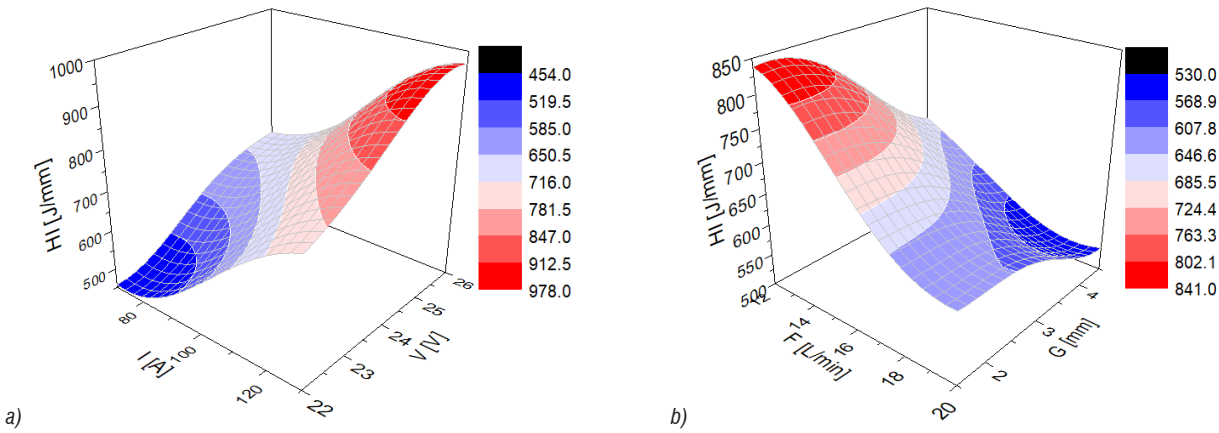

Fig. 8. *The impacts of process parameters on the HI; a) HI versus I and V, and b) HI versus F and G*

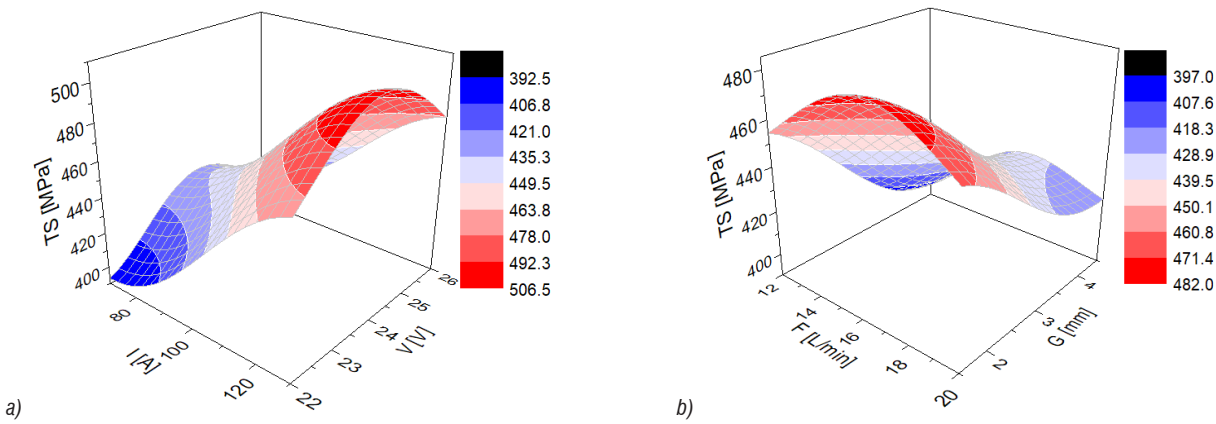

Fig. 9. *The impacts of process parameters on the TS; a) TS versus I and V, and b) TS versus F and G*

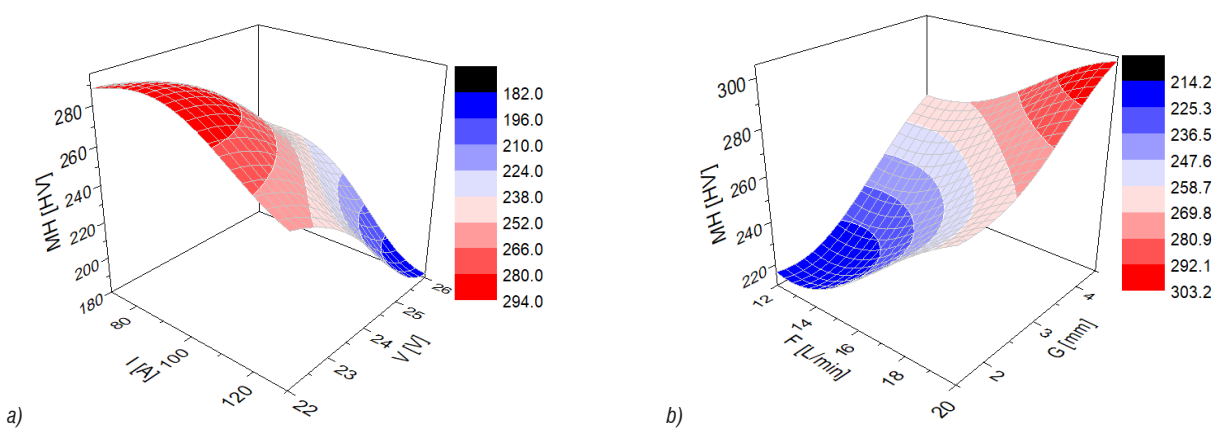

Fig. 10. The impacts of process parameters on the *MH*; *MH* versus *I* and *V*, and b) *MH* versus *F* and *G*

respectively. The contributions of the I^2, V^2, F^2, and G^2 are 4.51 %, 3.18 %, 3.68 %, and 4.12 %, respectively. As a result, the *I* is the most effective factor, followed by the *V, F,* and *G*, respectively.

ANOVA results for the *TS* model are shown in Table 5. The *I, V, F, G, IV, IF, IG, VG, FG,* I^2, V^2, F^2, and G^2 are significant terms for the *HI* model. The contributions of the *I, V, F,* and *G* are 22.18 %, 3.79 %, 5.15 %, and 15.16 %, respectively. The contributions of the *IV, IF, IG, VG*, and *FG* are 2.01 %, 1.31 %, 3.93 %, 1.45 %, and 2.32 %, respectively. The contributions of the I^2, V^2, F^2, and G^2 are 4.43 %,

18.17 %, 14.82 %, and 4.74 %, respectively. As a result, the *I* is the most effective factor, followed by the *G, F*, and *V*, respectively.

Table 4. *ANOVA results for the HI model*

So	*SS*	*MS*	*F* Value	*p*-value
Model	424549.38	30324.96	41.02	< 0.0001
I	380583.72	380583.72	514.77	< 0.0001
V	262248.10	262248.10	354.71	< 0.0001
F	226952.03	226952.03	306.97	< 0.0001
G	189609.81	189609.81	256.46	< 0.0001
IF	58485.76	58485.76	79.11	0.0072
IG	246219.93	246219.93	333.03	< 0.0001
FG	65306.26	65306.26	88.33	0.007
I^2	76901.10	76901.10	104.01	0.0062
V^2	54222.95	54222.95	73.34	0.0071
F^2	62748.57	62748.57	84.87	0.0071
G^2	70251.12	70251.12	95.02	0.0064
Res.	10350.62	739.33		
Cor.	434900.00			
R^2 = 0.9762; Adj. R^2 = 0.9612; Pre. R^2 = 0.9536				

Table 5. *ANOVA results for the TS model*

So	*SS*	*MS*	*F* Value	*p*-value
Model	19509.10	1393.51	49.50505051	< 0.0001
I	19830.89	19830.89	704.47	< 0.0001
V	3388.60	3388.60	120.38	< 0.0001
F	4577.74	4577.74	162.62	< 0.0001
G	13554.39	13554.39	481.51	< 0.0001
IV	1797.12	1797.12	63.84	0.0062
IF	1171.26	1171.26	41.61	0.0094
IG	3513.77	3513.77	124.82	0.0034
VG	1296.43	1296.43	46.05	0.0096
FG	2074.29	2074.29	73.69	0.0058
I^2	3960.81	3960.81	140.70	< 0.0001
V^2	16728.41	16728.41	594.26	< 0.0001
F^2	13250.40	13250.40	470.71	< 0.0001
G^2	4237.98	4237.98	150.55	< 0.0001
Res.	394.08	28.15	3176.16	
Cor.	19903.18			
R^2 = 0.9802; Adj. R^2 = 0.9724; Pre. R^2 = 0.9602				

ANOVA results for the MH model are shown in Table 6. The *I, V, F, G, IV, IF, VF, VG, FG,* I^2, V^2, F^2, and G^2 are significant terms. The contributions of the *I, V, F*, and *G* are 15.66 %, 16.28 %, 15.05 %, and 12.29 %, respectively. The contributions of the *IV, IF, VF, VG,* and *FG* are 3.33 %, 8.85 %, 1.79 %, 2.38 %, and 1.74 %, respectively. The contributions of the I^2, V^2, F^2, and G^2 are 9.46 %, 4.91 %, 3.82 %, and 4.27 %, respectively.

Table 6. *ANOVA results for the MH model*

So	*SS*	*MS*	*F* Value	*p*-value
Model	25581.89	1827.28	38.68	< 0.0001
I	32604.92	32604.92	690.20	< 0.0001
V	33895.79	33895.79	717.52	< 0.0001
F	31334.87	31334.87	663.31	< 0.0001
G	25588.41	25588.41	541.67	< 0.0001
IV	6933.23	6933.23	146.77	0.0012
IF	18426.15	18426.15	390.05	< 0.0001
VF	3726.87	3726.87	78.89	0.0024
VG	4955.28	4955.28	104.90	0.0019
FG	3622.77	3622.77	76.69	0.0026
I^2	19696.20	19696.20	416.94	< 0.0001
V^2	10222.87	10222.87	216.40	< 0.0001
F^2	7953.43	7953.43	168.36	< 0.0001
G^2	8890.36	8890.36	188.20	< 0.0001
Res.	661.33	47.24	4407.39	
Cor.	26243.22			
R^2	0.9748			
R^2 = 0.9748; Adj. R^2 = 0.9742; Pre. R^2 = 0.9586				

Table 7 presents confirmations of the precision of the *HI, TS*, and *MH* models. The small deviations (less than 5 %) indicate the allowable validity of the RBFN correlations.

3.3 Optimal Outcomes Produced by the ANSGA-II

The weights of the *HI, TS*, and *MH* are 0.36, 0.33, and 0.31, respectively. Fig. 11 shows the Pareto graphs produced by ANSGA-II. Consequently, a low *HI* causes a reduction in the *TS* (Fig. 11a), while a larger *HI* results in an enhanced *MH* (Fig. 11b). Accordingly, the optimal point with the highest PI_i is chosen as the best one (Table 8). The best results produced by the *I, V, F*, and *G* are 89 A, 23 V, 20 L/min, and 1.5 mm, respectively (Table 10). Whereas the *TS* and *MH* are improved by 1.2 % and 19.8 %, respectively, the *HI* is down 18.4 %.

3.4 Optimal Outcomes Produced by the NSGA-II

To prove the strength of the proposed approach, the conventional NSGA-II is applied to find optimal data. The optimal values of the *I, V, F*, and *G* are 81 A, 22 V, 19 L/min, and 1.4 mm, respectively (Table 8). The corresponding values of the *HI, TS*, and *MH* are

Table 7. *Comparative data for RBFN models*

No.	*HI* [J/mm]			*TS* [MPa]			*MH* [HV]		
	Actual	Pre.	Error	Actual	Pre.	Error	Actual	Pre.	Error
33	411.09	409.56	0.37	398.31	397.36	0.24	364.2	366.7	-0.69
34	711.62	709.62	0.28	424.53	426.56	-0.48	272.4	274.4	-0.73
35	739.42	741.86	-0.33	455.12	453.21	0.42	271.8	269.3	0.92
36	804.95	806.32	-0.17	467.22	465.98	0.27	268.6	266.7	0.71
37	649.06	650.38	-0.20	452.62	454.82	-0.49	302.3	304.6	-0.76
38	524.92	522.94	0.38	421.51	419.36	0.51	329.2	331.2	-0.61
39	741.25	739.62	0.22	414.83	416.85	-0.49	266.1	268.5	-0.90
40	769.22	771.25	-0.26	474.26	476.29	-0.43	263.7	265.4	-0.64
41	779.18	777.36	0.23	459.98	461.32	-0.29	267.5	265.4	0.79
42	450.74	452.23	-0.33	408.81	410.39	-0.39	351.7	349.6	0.60
43	629.07	628.36	0.11	440.35	438.36	0.45	316.3	318.4	-0.66
44	803.78	805.24	-0.18	456.12	458.81	-0.59	252.2	254.3	-0.83
44	748.98	750.66	-0.22	467.86	465.39	0.53	283.3	281.2	0.74
45	851.04	850.36	0.08	479.81	481.25	-0.30	270.4	272.6	-0.81
46	778.37	779.86	-0.19	442.05	446.08	-0.91	251.8	249.6	0.87
47	688.59	690.46	-0.27	444.37	446.52	-0.48	283.4	285.6	-0.78

Table 8. *Optimization results produced by the ANSGA-II and NSGA-II*

Method	Optimization parameters				Responses			I_i
	I [A]	*V* [V]	*F* [L/min]	*G* [mm]	*HI* [J/mm]	*TS* [MPa]	*MH* [HV]	
Initial values	100	25	15	3.0	764.35	449.47	264.6	
ANSGA-II	89	23	20	1.5	623.46	454.77	317.1	0.936
NSGA-II	81	22	19	1.4	638.31	450.22	316.8	0.869
Improvement by ANSGA-II [%]					-18.4	+1.2	+19.8	

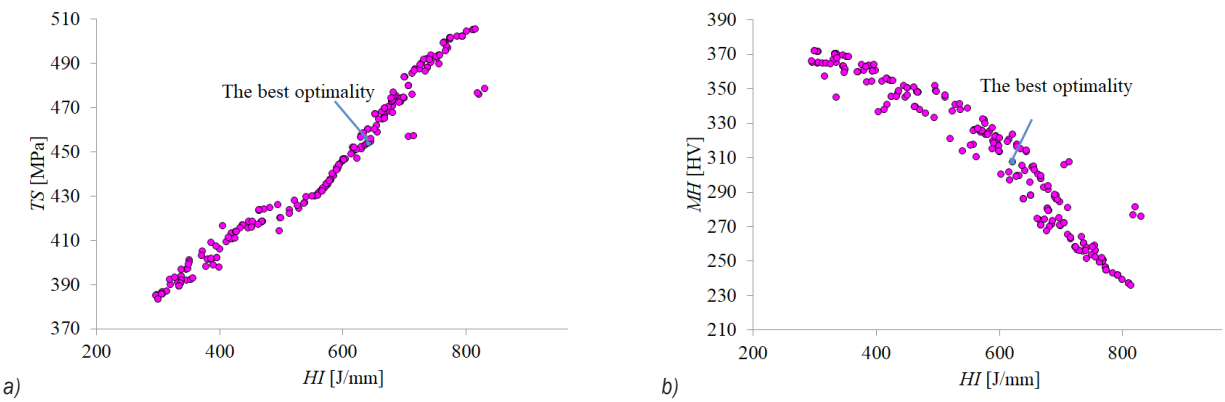

a) b)

Fig. 11. *Pareto fronts generated by ANSGA- II; a) HI versus TS, and b) HI versus MH*

638.31 J/mm, 450.22 MPa, and 316.8 HV. However, the conventional NSGA-II provides a higher *HI* and lower *TS,* as well as *MH*. In comparison to the traditional NSGA-II, it can be stated that the ANSGA-II produces superior optimal results.

3.5 Novelty and Applications of the Findings

The novelty of this work can be expressed as follows.

This work proposed an efficient optimizing algorithm entitled ANSGA-II, which could be effectively applied to solve complicated issues and find global results instead of traditional algorithms.

The trade-off analysis between the *HI*, *TS*, and *MH* was successfully solved using optimal parameters.

The optimality can be used to obtain a sustainable GTAW process.

The highly accurate models of the *HI*, *TS*, and *MH* were developed using the ANN approach, as compared to the conventional RSM ones.

The proposed optimization technique comprising RBFN-ANSGA-II-EAMR can be used to address optimization problems related to various GTAW operations and machining processes.

The applications of the findings can be expressed as follows.

The findings can be utilized to develop an expert system that will allow the GTAW to operate in many industries.

The practical *HI, TS*, and *MH* values of the GTAW Ti40A can be predicted using the RBFN models.

The optimal data can be utilized to improve quality indicators and energy efficiency of the practical GTAW Ti40A.

By leveraging the effects of GTAW inputs on the output, the technological knowledge of the GTAW process can be improved significantly.

The range of output objectives may be considered crucial technical advice for welding researchers.

4 CONCLUSIONS

The objective of the current study was to select the optimal GTAW inputs (*I*, *V*, *F*, and *G*) in order to decrease heat input (*HI*) and increase welding quality (*TS* and *MH*). The ANSGA-II was utilized to produce feasible solutions, and the RBFN method was applied to recommend GTAW solutions. The WPCA and EAMR were applied to calculate the weights and select the best optimal results. The conclusions are presented as follows:

1. The highest *F* and *G* values were recommended, but to reduce the *HI*, the low values of *I* and *V* were used. The medium values of *V* and *F* were addressed, and the highest *I* and lowest *G* were utilized to improve the *TS*. The lowest *I* and *V* were utilized, while the highest *F* and *G* were used to optimize the *MH*.
2. The *HI, TS*, and *MH* increase from 388.56 J/mm to 980.14 J/mm, 388.73 MPa to 530.87 MPa, and 319.3 HV to 364.2 HV, respectively, for the GTAW parameters considered.
3. The *I* and *V* contributed the most to the *HI* and *MH* models. The *I* and *G* were named as the most effective parameter in the *TS* model.
4. The *I, V, F*, and *G* have optimal data of 89 A, 23 V, 20 L/min, and 1.5 mm, in that order. While the *HI* was saved by 18.4 %, the *TS* and *MH* improved by 1.2 % and 19.8 %, respectively.
5. The Pareto graphs produced by the ANGA-II could be used to select optimal parameters and responses for different GTAW purposes.
6. Compared to the conventional NSGA-II, the developed ANSGA-II might be used to tackle complex problems and produce better results.
7. The ANSGA-II could be utilized to obtain global data instead of conventional algorithms.
8. The designed and fabricated fixture can be utilized in other GTAW operations.
9. Improving *HI, TS*, and *MH* are practical benefits to the GTAW Ti40A operation.
10. The impacts of the GTAW factors on air pollution and elongation will be explored in future work.

5 REFERENCES

[1] Sonar, T., Balasubramanian, V., Malarvizhi, S., Venkateswaran, T., Sivakumar, D. (2020). Multi-response mathematical modelling, optimization and prediction of weld bead geometry in gas tungsten constricted arc welding (GTCAW) of Inconel 718 alloy sheets for aero-engine components. *Multiscale and Multidisciplinary Modeling, Experiments and Design*, vol. 3, p. 201-226, **DOI:10.1007/s41939-020-00073-3**.

[2] Sivakumar, J., Vasudevan, M., Korra, N.N. (2020). Systematic welding process parameter optimization in activated tungsten inert gas (A-TIG) welding of Inconel 625. *Transactions of the Indian Institute of Metals*, vol. 73, p. 555-569, **DOI:10.1007/s12666-020-01876-1**.

[3] Karpagaraj, A., Rajesh Kumar, N., Thiyaneshwaran, N., Siva Shanmugam, N., Cheepu, M., Sarala, R. (2020). Experimental and numerical studies on gas tungsten arc welding of Ti-6Al-4V tailor-welded blank. *Journal of the Brazilian Society of Mechanical Sciences and Engineering*, vol. 42, p. 532, **DOI:10.1007/s40430-020-02629-3**.

[4] Sivakumar, J., Korra, N.N. (2021). Optimization of welding process parameters for activated tungsten inert welding of Inconel 625 Using the technique for order preference by similarity to ideal solution methodology. *Arabian Journal for Science and Engineering*, vol. 46, p. 7399-7409, **DOI:10.1007/s13369-021-05409-w**.

[5] Omprakasam, S., Marimuthu, K., Raghu, R., Velmurugan, T. (2022). Statistical modelling and optimization of TIG welding process parameters using Taguchi's method. *Strojniški vestnik - Journal of Mechanical Engineering*, vol. 68, no. 3, p. 200-209, **DOI:10.5545/sv-jme.2021.7414**.

[6] Moghaddam, M.A., Kolahan, F. (2022). Modeling and optimization of A-GTAW process using Box-Behnken design and hybrid BPNN-PSO approach. *Proceedings of the Institution of Mechanical Engineers, Part E: Journal of Process Mechanical Engineering*, vol. 236, no. 3, p. 859-869, **DOI:10.1177/09544089211050457**.

[7] Wan, Z., Meng, D., Zhao, Y., Zhang, D., Wang, Q., Shan, J., Song, J., Wang, G., Wu, A. (2021). Improvement on

the tensile properties of 2219-T8 aluminum alloy TIG welding joint with weld geometry optimization. *Journal of Manufacturing Processes*, vol. 67, p. 275-285, **DOI:10.1016/j.jmapro.2021.04.062**.

[8] Vijayakumar, V., Sonar, T., Venkatesan, S., Negemiya, A., Ivanov, M. (2024). Influence of IP-TIG welding parameters on weld bead geometry, tensile properties, and microstructure of Ti6Al4V alloy joints. *Materials Testing*, **DOI:10.1515/mt-2023-0237**.

[9] Sonar, T., Balasubramanian, V., Malarvizhi, S., Venkateswaran, T., Sivakumar, D. (2021). Maximizing strength and corrosion resistance of InterPulsed TIG welded Superalloy 718 joints by RSM for aerospace applications. *CIRP Journal of Manufacturing Science and Technology*, vol. 35, p. 474-493, **DOI:10.1016/j.cirpj.2021.07.013**.

[10] Sonar, T., Balasubramanian, V., Malarvizhi, S., Venkateswaran, T., Sivakumar, D. (2020). Development of 3-Dimensional (3D) response surfaces to maximize yield strength and elongation of InterPulsed TIG welded thin high temperature alloy sheets for jet engine applications. *CIRP Journal of Manufacturing Science and Technology*, vol. 31, p. 628-642, **DOI:10.1016/j.cirpj.2020.09.003**.

[11] Singh, B.K., Chauhan, N., Mishra, A.K., Yadhuvanshi, A.A., Kumar, A., Ansu, A.K., Goyal, A. (2023). Experimental investigation of welding parameters to enhance the impact strength using gas tungsten arc welding. *International Journal on Interactive Design and Manufacturing*, **DOI:10.1007/s12008-023-01264-1**.

[12] Baek, D., Moon, H.S., Park, S.H. (2024). Optimization of weld penetration prediction based on weld pool image and deep learning approach in gas tungsten arc welding. *International Journal of Advanced Manufacturing Technology*, vol. 130, p. 2617-2633, **DOI:10.1007/s00170-023-12855-3**.

[13] Baskoro, A.S., Widyianto, A., Prasetyo, E., Kiswanto, G. (2024). The Taguchi and response surface method for optimizing orbital pipe welding parameters in pulsed current gas tungsten arc welding (PC-GTAW) for SS316L. *Transactions of the Indian Institute of Metals*, **DOI:10.1007/s12666-023-03254-z**.

[14] Baek, D., Moon, H.S., Park, S.H. (2024). In-process prediction of weld penetration depth using machine learning-based molten pool extraction technique in tungsten arc welding. *Journal of Intelligent Manufacturing*, vol. 35, p. 129-145, **DOI:10.1007/s10845-022-02013-z**.

[15] Pandya, D., Badgujar, A., Ghetiya, N., Oza, A.D. (2022). Characterization and optimization of duplex stainless steel welded by activated tungsten inert gas welding process. *International Journal on Interactive Design and Manufacturing*, **DOI:10.1007/s12008-022-00977-z**.

[16] Baskoro, A.S., Amat, M.A., Widyianto, A., Putra, A.D., Aryadhani, S.A. (2024). Investigation of weld geometry, mechanical properties, and metallurgical observations of activated flux tungsten inert gas (A-TIG) welding on 304 austenitic stainless steel. *Transactions of the Indian Institute of Metals*, vol. 77, p. 897-906, **DOI:10.1007/s12666-023-03180-0**.

[17] Elangandhi, J., Periyagounder, S., Selavaraj, M., Saminatharaja, D. (2023). Mechanical and microstructural properties of B4C/W reinforced copper matrix composite using a friction stir-welding process. *Strojniški vestnik - Journal of Mechanical Engineering*, vol. 69, no. 9-10, p. 388-400, **DOI:10.5545/sv-jme.2023.518**.

[18] Ibrahim, M.A., Çamur, H., Savaş, M., Sabo, A.K. (2022). Multi-response optimization of the tribological behaviour of PTFE-based composites via Taguchi grey relational analysis. *Strojniški vestnik - Journal of Mechanical Engineering*, vol. 68, no. 5, p. 359-367, **DOI:10.5545/sv-jme.2021.7466**.

[19] Singh, V., Chandrasekaran, M., Samanta, S., Devarasiddappa, D., Arunachalam, R. (2021). Sustainability assessment of gas metal arc welding process of AISI 201LN using AHP-TLBO integrated optimization methodology. *Journal of the Brazilian Society of Mechanical Sciences and Engineering*, vol. 43, art. ID 68, **DOI:10.1007/s40430-020-02786-5**.

[20] Bhattacharya, A., Singla, S. (2017). Dissimilar GTAW between AISI 304 and AISI 4340 steel: Multi-response optimization by analytic hierarchy process. *Proceedings of the Institution of Mechanical Engineers, Part E: Journal of Process Mechanical Engineering*, vol. 231, no. 4, p. 824-835, **DOI:10.1177/0954408916641458**.